Journal of Materials Chemistry A

Accepted Manuscript

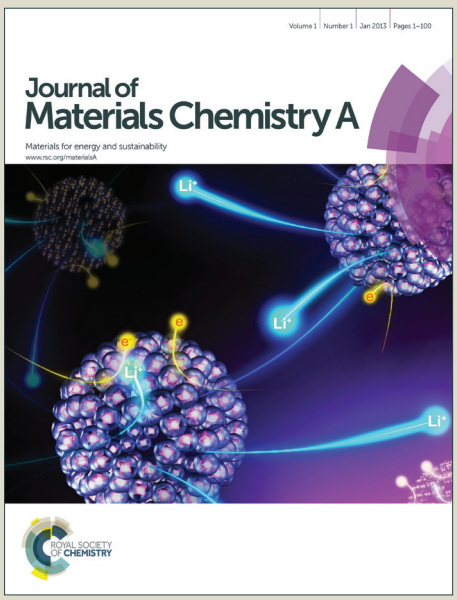

ROYAL SOCIETY OF CHEMISTRY

www.rsc.org/materialsA

Journal of Materials Chemistry A

PAPER

Controlled synthesis of three-dimensional interconnected graphene-like nanosheets from graphite microspheres as high-performance anodes for lithium-ion batteries

Received 00th January 20xx,
Accepted 00th January 20xx

DOI: 10.1039/x0xx00000x

www.rsc.org/

Hong-Qiang Wang[a], Guan-Hua Yang[a], Li-San Cui[a], Ze-Sheng Li[b,*], Zhi-Xiong Yan[a], Xiao-Hui Zhang[a], You-Guo Huang[a] and Qing-Yu Li[a,*]

Three-dimensional (3D) graphene-based materials have received increasing attention due to their application potential in electrochemical energy storage and conversion. Herein, we demonstrate a facile and efficient strategy to synthesize 3D interconnected graphene-like nanosheets (3DGNs) directly developed from graphite microspheres. The graphene-like nanosheets are interwoven into unique 3D macroporous network architecture, which can prevent the graphene nanosheets from aggregating effectively. When used as an anode in lithium ion batteries, the 3DGNs architecture is capable of reaching an extremely high reversible discharge capacity of 2795.6 mAh/g, while maintaining a good electrochemical stability with a very high capacity of 1708.5 mAh/g after 120 cycles. The superior electrochemical performances of the 3DGNs architecture may be attributed to the unique structure features, such as the efficient ions/electrons conductive channels of 3D interconnected nanosheets, enhanced specific surface area as well as their favorable surface structural features.

Introduction

With the development of science and technology, especially the popularization of electronic products, people's life has been greatly improved. As an important component of the electronic products, lithium ion batteries (LIBs) play an increasingly important role in modern world. In recent years, due to the rapid development of electric vehicles and hybrid electric vehicles, the requirement in developing LIBs with high capacity and high energy density is becoming more and more prominent.[1] The research on the anode material is very important for the development of the LIBs in the electric power-type application. However, traditional commercial graphite anode materials with a low theoretical capacity of 372 mAh/g offer a very limited energy output for LIBs, and alternative anode materials with higher capacity and higher energy density are highly desirable.[2] Recently, a new-style two-dimensional graphite material, graphene, has attracted great attention and has been widely regarded as a potential candidate to replace traditional graphite for high-performance LIB anode,[3] owing to its outstanding electrical conductivity, good mechanical flexibility, large specific surface area, as well as high thermal/chemical stability. Nevertheless, the practical discharge specific capacity of individual graphene nanosheets (e.g. reduced graphene oxide nanosheets) is not come up to anticipated data, since the irreversible aggregation or re-stacking of graphene nanosheets by the strong van der Waals forces.[4] Fortunately, the newly developed three-dimensional (3D) graphene architectures have demonstrated an attractive prospect to overcome the above problems.[5] The unique 3D graphene architectures often possess a macroporous network of interconnected graphene nanosheets, which can prevent the graphene nanosheets from aggregating effectively.[6] Besides, such interconnected and macroporous architectures provide versatile binary channels for the electron transport and diffusion of ions.[7] So significantly improved energy storage performance for 3D graphene materials can be achieved for electrochemical systems.[8]

Currently, the design and synthesis of 3D graphene architectures can be generalized as two basic strategies:[9] (1) "top-down" chemical exfoliation of graphite into graphene nanosheets and subsequent self-assembly into 3D framework; (2) directly "bottom-up" catalytic graphitization from gaseous or solid carbon sources with controlled orientation. With regard to the first strategy, for the first time, Shi and co-workers accomplished the preparation of 3D self-assembled graphene network by a hydrothermal reduction of graphene oxide.[10] This study opens a way for extensive production of 3D graphene and its composite networks through the hydrothermal reduction route.[11] Template-guided self-assembly is also an effective method for the construction of 3D graphene architectures. For example, Choi and

[a] *Guangxi Key Laboratory of Low Carbon Energy Materials, School of Chemical and pharmaceutical Sciences, Guangxi Normal University, Guilin, 541004, China*

[b] *Development Center of Technology for Petrochemical Pollution Control and Cleaner Production of Guangdong Universitites, College of Chemical Engineering, Guangdong university of Petrochemical Technology, Maoming, Guangdong, 525000, China*

Corresponding authors
E-mail addresses:
** Qing-Yu Li, liqingyu62@126.com Fax: +86-0773-5858562*
** Ze-Sheng Li, lzs212@163.com*
† Footnotes relating to the title and/or authors should appear here.
Electronic Supplementary Information (ESI) available: [details of any supplementary information available should be included here]. See DOI: 10.1039/x0xx00000x

co-workers reported the preparation of 3D graphene macroporous structure from graphene oxide with polystyrene microspheres as templets.[12] With regard to the second strategy, the most successful case should be the nickel foam-oriented catalytic graphitization. Recently, the Cheng et al. pioneered a chemical-vapor-deposition synthesis of self-supported 3D graphene foam by using nickel foam as template and catalytic medium.[13] More recently, Li et al. reported the synthesis of 3D graphene-like (ultrathin graphite sheet) networks by nickel particles as catalyst from the solid carbon source of resin.[14] It is noteworthy that such 3D networks made up of graphene-like nanosheets show attractive application prospect due to their scalable synthesis and promising properties in energy storage.

Generally, the previously reported 3D graphene architectures are preferably used as the active electrodes for flexible supercapacitors, conductor for stretchable electronics, catalysis support and materials of hydrogen storage, while rarely used as active electrodes for high-performance LIBs.[6] There are at least two reasons why the existing 3D graphene architectures are not suitable for advanced applications of LIBs: (1) the most reported 3D graphene architectures are focused on the design of macroscopic materials (e.g. foams, sponges and aerogels) in centimeter scale, which are difficult for the making of feasible electrodes for LIBs; (2) the pores in previous 3D graphene architectures are in the range of hundreds of nanometers to several micrometers, where the extremely increased volume of materials has been a inevitable obstacle for acquiring high volume energy density. As suggested above, the processability and dispersibility of the 3D graphene architectures become a matter of prime importance for the fabrication of practicable electrodes for LIBs. Fortunately, the design style of 3D graphene-like micro-architectures (powders in about ten micrometer[14]) could resolve this problem to a large degree. Because the 3D graphene-based micropowders not only prevent restacking of graphene nanosheets but also can be easily processed onto the anode current collector (namely copper film) by the mature and fashionable coating technique.[15] Significantly, these strategies could be capable of providing a high energy density for LIBs.

In this investigation, we present the controlled synthesis of newly three-dimensional interconnected graphene-like nanosheets (3DGNs) from one commercial graphite microspheres, graphited mesocarbon microbeads (GMCMBs). Expressly, an efficient chemical oxidation-thermal expansion united strategy was introduced for straightforward evolvement of GMCMBs into 3DGNs, without the help of additional self-assembly or templet-orientation processes. The present 3DGNs architectures have several obvious structural features: (i) excellent micropowder structure is succeeded from the precursor of GMCMBs, (ii) these graphene-like nanosheets are well interconnected into 3D network structure, (iii) relatively suitable and uniform macroporous structure in hundreds of nanometers is achieved. With these merits, we demonstrate that the anode for LIBs with high capacity and high energy density can be designed based on the 3DGNs architectures.

Experimental

Synthesis of materials

The GMCMB is purchased from Shenzhen Beiterui new energy materials co., Ltd in China. The other chemicals are purchased from West Long Chemical co., Ltd in China. In a typical synthesis of 3D graphene-like nanosheets samples (3DGNs), GMCMB (8 g), $NaNO_3$ (2.5 g) and H_2SO_4 (200 mL) were mixed and stronglystirred for 15 min in a 1000 Ml three-necked flask. Afterwards, $KMnO_4$ (10 g) was added slowly to the above solution and strongly stirred at 4 ^oC for 3 h. After this, the mixture was stirred at 35^oC for 3 h and then added into 400 mL of 80 ^oC distilled water. The temperature of the solution was slowly heated to 95^oC and then 100 mL of H_2O_2 (10%) was added to the mixture to reduce residual permanganate. The solution was stirred continuously for 5 h and the mixture was filtered and washed with HCl aqueous solution (10 wt.%), followed by repeated washings with distilled water to reach a pH value of 7.0. The resultant black precipitate was dried at 80 ^oC in the oven and then quickly placed in a pre-heated tube furnace (950 ^oC) expanding for 10 min in high purity argon atmosphere. After that, the black precipitate was rapidly removed from the tube furnace to cool. The as-prepared sample was designated as 3DGNs (10g) (10g denotes that 10 g $KMnO_4$ is used). As a comparison, 3DGNs (12g), 3DGNs (14g), 3DGNs (16g), 3DGNs (18g) was synthesized by the same steps with different dosages of $KMnO_4$. Special Notes: the optimized heated temperature of 950 ^oC is beforehand confirmed by the controlled experiments with different heating temperatures (850, 900, 950 and 1000 ^oC) but with the same $KMnO_4$ dosages of 10g.

Characterization of materials

The structure of the as-prepared samples were characterized by X-ray diffraction (XRD, Rigaku, D/max 2500v/pc) using Cu Kα radiation (λ= 0.15418 nm). Fourier transform infrared (FTIR) spectrometry was carried out to explore the functional groups of the samples by using the KBr disk technique. Raman spectra were collected with a laser Raman spectroscope (invia, Renishaw). The microstructure of the as-prepared samples were observed using field emission scanning electron microscopy (FESEM, Philips, FEI Quanta 200 FEG), and transmission electron microscope (TEM, Tokyo, Japan, JEOL 2100F). SEM equipped with an X-ray energy dispersive spectrometer (EDS, INCA) to analyze the composition of the sample. N_2 adsorption/desorption isotherms were investigated the specific surface area and pore-structural properties of material using an automatic volumetric sorption analyzer (SA3100 Beckman Coulter, USA) at liquid nitrogen temperature (77 K).

Electrode preparation and electrochemical measurements

The working electrodes were prepared by mixing with as-prepared samples, carbon black and polyvinylidene difluoride (PVDF) binder (80:10:10, w/w/w) in N-methyl-2-pyrrolidinone (NMP) to form a homogeneous slurry, which was homogeneously pasted onto a pure copper foil. After pressing, the prepared working electrodes were dried in a vacuum oven at 80 ^oC for 12 h and assembled in test cells (CR2032 coin type) in an argon-filled glove box with Li metal foil (Aldrich, USA) as the counter electrode. The electrolyte was composed of 1 mol L^{-1} $LiPF_6$ dissolved in a mixture of ethylene carbonate (EC)/diethyl carbonate (DEC) 1:1 (vol%). The galvanostatical discharge and charge tests were performed with a Battery Testing System (Land, Wuhan, China) using the voltage between 0.01 and 3.00 V at the current density of 100 mA g^{-1}.

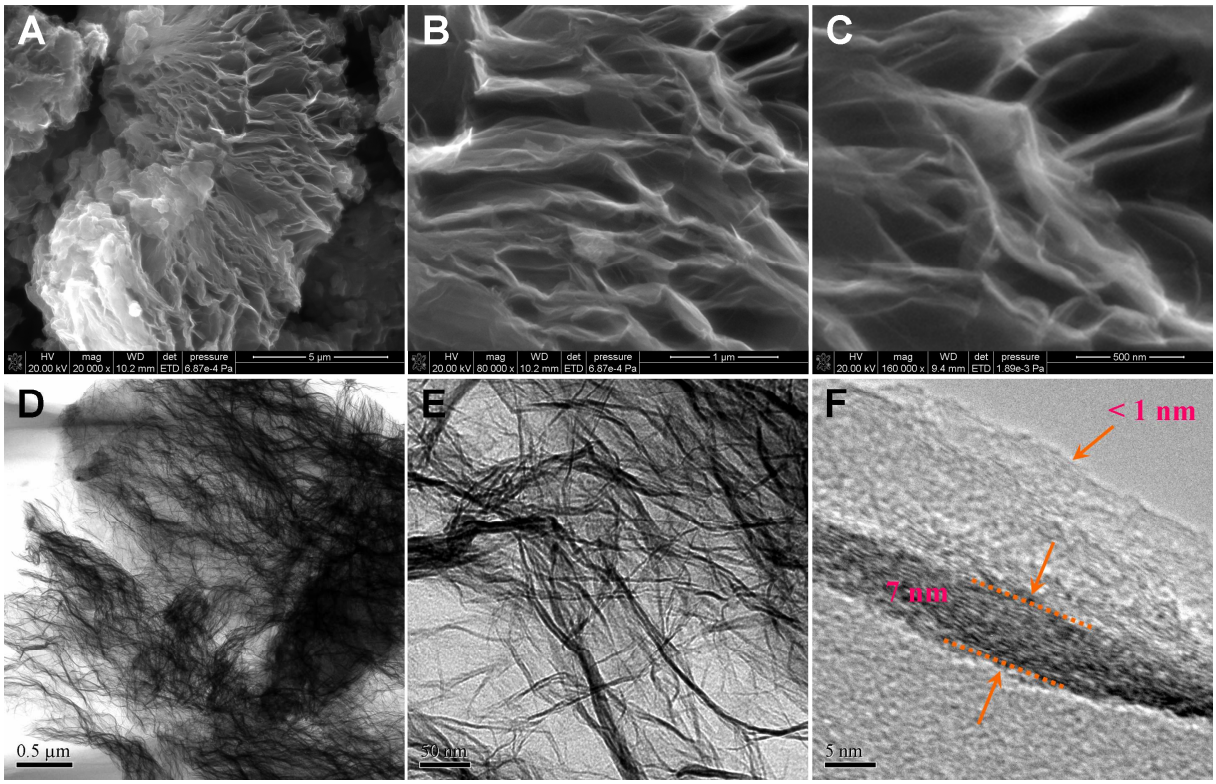

Fig. 1 Typical SEM images (A-C) and TEM images (D-F) of the 3DGNs ($KMnO_4$=18 g, heating temperature=950 °C).

Results and discussion

The microstructures of the 3DGNs were investigated by the SEM and TEM techniques, with the results shown in Fig. 1. The unique 3D micro-architectures made up of interconnected nanosheets can be observed from the SEM image in Fig. 1 A. It is important to note that the excellent micropowder structure of 3DGNs is succeeded from the precursor of GMCMBs (see Fig. S1). The magnified SEM images (Fig. 1 B and C) further exhibit an interconnected network with submicrometer sized macropores (the spacing of nanosheets is less than 500 nm) for 3DGNs. The walls of the interconnected 3D macroporous networks possess a clear curvy profile, which indicates a well mechanical flexibility of these nanosheets composed of a few graphene layers. The detailed nanostructures of 3DGNs were further studied by TEM and high-resolution TEM (HRTEM). The low magnification TEM images (Fig. 1 D and E) show the interwoven 3D network formed by the interconnection of these graphene-like nanosheets, which is in good agreement with the SEM observations. The semitransparent effects of these TEM images indicate that the 3DGNs should be of ultrathin nanostructures. As can be seen from HRTEM image (Fig. 1 F), the thickness of the graphene-like nanosheets consisting of a few graphene layers is about 7 nm in a folded pattern and less than 1nm at their borderline. In addition, the in-plane crystallinity of these graphene layers is also distinctly displayed by the HRTEM image. Above-mentioned results evidenced that desirable 3D architectures consisted of interconnected graphene-like nanosheets have been developed from the precursor of GMCMBs successfully by the efficient chemical oxidation-thermal expansion associated strategy.

The SEM-EDS mapping technique was further utilized to detect the element distribution and composition of the 3DGNs (see Fig. 2). Fig. 2 A-C presents the selected SEM image and EDS elemental mapping of C and O from the individual 3DGNs micro-architecture. It is found that the elements C and O (Fig. 2 B and C respectively) are homogeneously distributed on the basis of SEM image (Fig. 2 A). The analysis result of EDS spectra (Fig. 2 D) affirms that the sample contains C, O, and S elements with an atomic ratio of 66.85% : 31.94% : 1.11%. The sample contained high levels of oxygen group, suggesting that external oxygen atoms can be combined with carbon atoms to form C=O and C-O-C bonds (see the FT-IR for details in Fig. S2) in the oxidation and heating procedure.[16] The negligible S element in the sample is introduced by H_2SO_4.

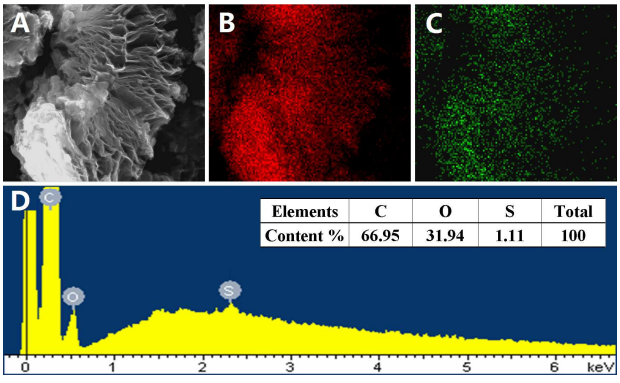

Fig. 2 SEM-EDS elemental mapping images (A-C) and EDS spectra (D) of the 3DGNs. A is the selected SEM image, B and C are EDS elemental mapping of C and O respectively. Inset in D is the composition proportion of the sample.

To show further insight into the evolution process and influential factors of the 3DGNs from precursor of GMCMBs, the controlled experiments with different heating temperature and different $KMnO_4$ dosage are implemented.

In the first place, controlled experiments with different heating temperatures (850, 900, 950 and 1000 ^oC) and the same $KMnO_4$ dosage of 10g were carried out. The optimized temperature is confirmed as 950 ^oC based on the results of material characterization and performance testing (see Fig. 3-5). Fig. 3 shows the SEM images of the samples with different heating temperatures (A:850, B:900, C:950 and D:1000 ^oC) and the same $KMnO_4$ dosage of 10g. Obviously, the samples with 850 and 900 ^oC have fewer cracks, and the sample with 950 ^oC has more cracks while the sphere structure remains intact. For the sample with 1000 ^oC, however, the sphere structure is badly damaged, which is not suitable for the construction of three-dimensional nanosheets micropowders. Fig. 4 and 5 show the galvanostatic charge/discharge profiles and discharge cycling profiles of the samples with different heating temperatures and the same $KMnO_4$ dosage of 10g. Obviously, the sample with 950 ^oC has the more excellent electrochemical performances with higher reversible discharge capacity of 567.8 mAh/g and 465.4 mAh/g after fifth cycles.

In the second place, controlled experiments with different $KMnO_4$ dosages (10g, 12g, 14g, and 16g) and the same heating temperature 950 ^oC were further operated. It is worthwhile that the $KMnO_4$ dosage is a critical factor for the development of 3D interconnected graphene-like nanosheets from the precursor graphite microspheres. In order to analyze the influence of material structures on the lithium storage performances, the as-prepared samples synthesized at 950 ^oC with different $KMnO_4$ dosages are systematically characterized by XRD, Raman spectrums, FT-IR, SEM, as well as nitrogen adsorption/desorption techniques. At the same time, the lithium storage performances of these samples are also systematically investigated by galvanostatic charge/discharge and electrochemical impedance spectroscopy techniques.

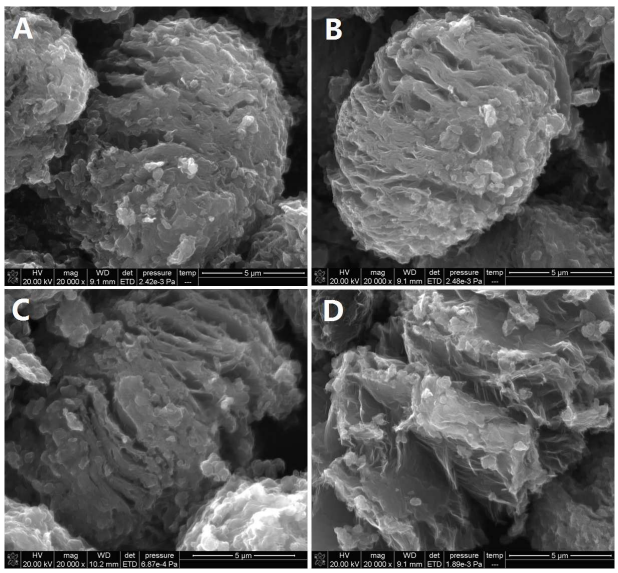

Fig. 3 Typical SEM images of the samples with different heating temperatures (A:850, B:900, C:950 and D:1000 ^oC) and the same $KMnO_4$ dosage of 10g.

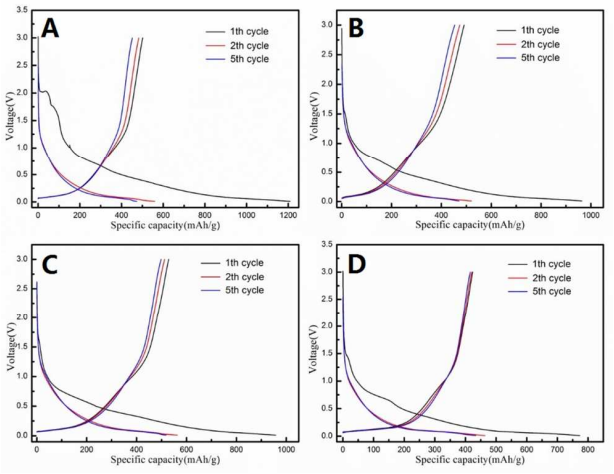

Fig. 4 Galvanostatic charge/discharge profiles of the samples with different heating temperatures (A:850, B:900, C:950 and D:1000 ^oC) and the same $KMnO_4$ dosage of 10g.

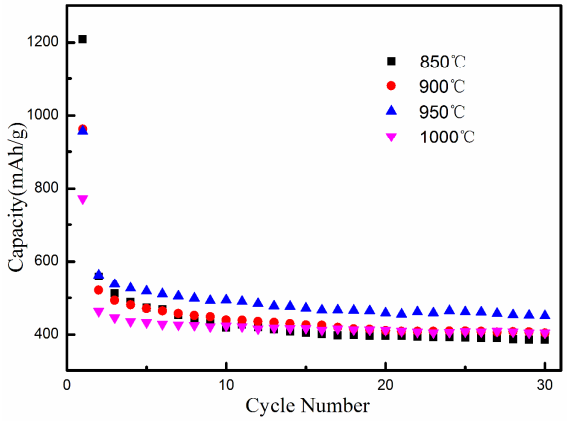

Fig. 5 Discharge cycling profiles of the samples with different heating temperatures and the same $KMnO_4$ dosage of 10g.

Fig. 6 shows the XRD patterns of the GMCMBs (Fig. 6 A) and 3DGNs (Fig. 6 B) treated with different $KMnO_4$ dosages at the same heating temperature of 950 ^oC. Obviously, the GMCMBs sample has a strong and narrow characteristic diffraction peak at about 26° (the crystal plane index is (002)). Meanwhile, the characteristic diffraction peaks of (100) and (101) crystal planes at about 42° and 44° are also clear and visible. All the results demonstrate the good crystallinity as well as high graphitization degree of the GMCMBs sample.[17] According to the arrangement of graphene layer, GMCMBs usually contain parallel, onion arrangement, meridian arrangement and other types, where the parallel type is the is the dominant model (see the inset in Fig. 6 A). After the GMCMBs (8 g) were treated with 10 g $KMnO_4$ and heated at 950 ^oC, the characteristic diffraction peak at about 26° (002) is also strong and the characteristic diffraction peaks at about 42° and 44° are also obvious. However, when $KMnO_4$ raised to 12 g, the intensity of (002) plane diffraction peak becomes much lower, and the diffraction peaks at about 42° and 44° are not obvious. All these diffraction peaks become increasingly weaker with the increasing $KMnO_4$ dosages. Expressly, the diffraction peaks of (100) and (101)

crystal planes almost disappeared when the dosage of $KMnO_4$ was raised to 18 g. These results indicate that, in the process of oxidation, the more oxidizing agents used, the more intercalator can inserted into the internal structure of graphite. Therefore, the crystal structure of graphite was sufficiently destroyed and potential graphene sheets can be grown during the reduction process at high temperature.[18]

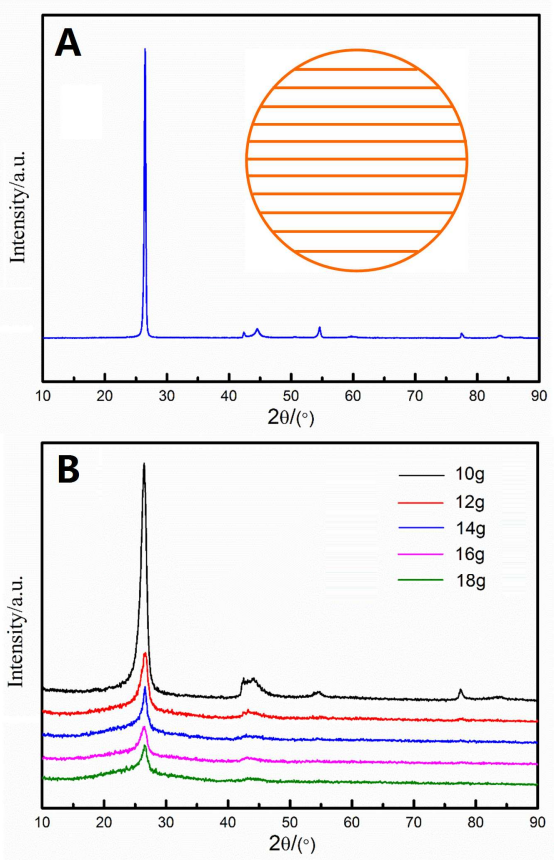

Fig. 6 XRD patterns of GMCMBs (A) and 3DGNs (B) treated with different $KMnO_4$ dosages at the same heating temperature of 950 °C.

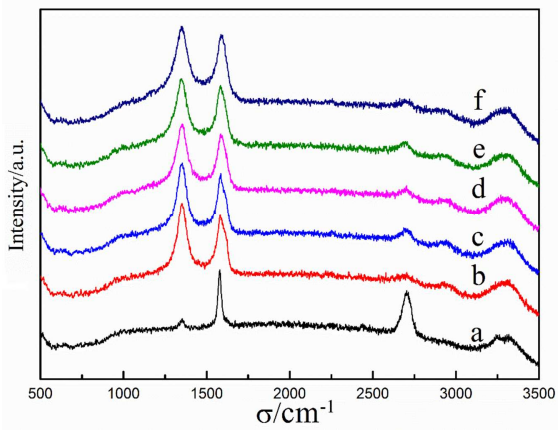

Fig. 7 Raman spectrums of GMCMBs (a) and 3DGNs (b-f) treated with different $KMnO_4$ dosages (b: 10 g, c: 12 g, d: 14 g, e: 16 g, f: 18 g) at the same heating temperature of 950 °C.

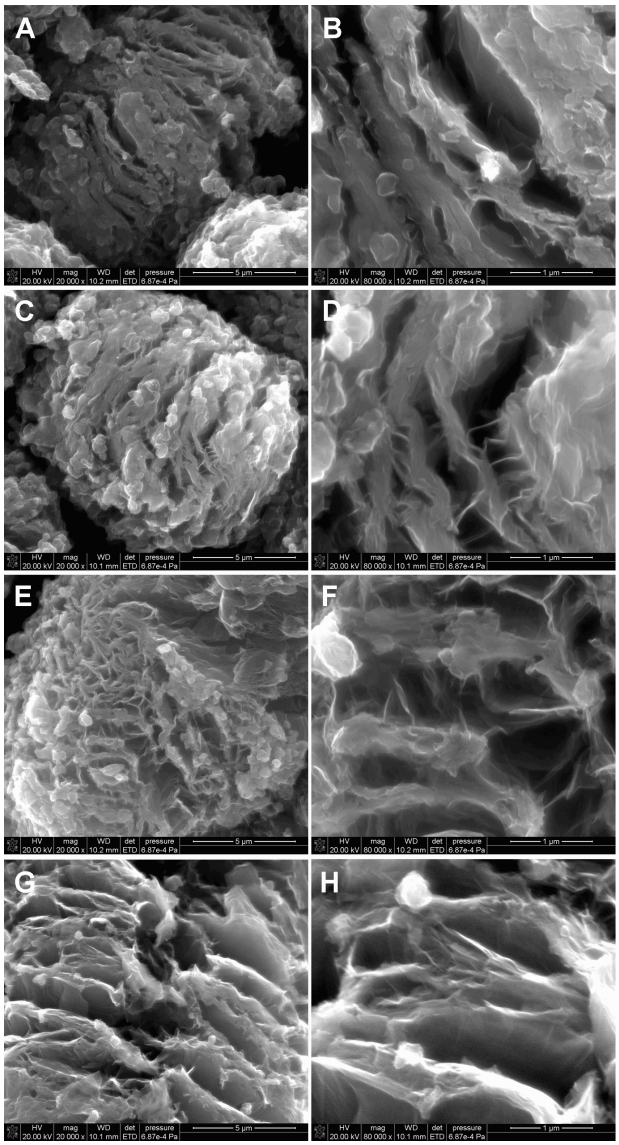

Fig. 8 SEM images of 3DGNs treated with different $KMnO_4$ dosages (A, B: 10 g, C, D: 12 g, E, F: 14 g, G, H: 16 g) at the same heating temperature of 950 °C.

Fig. 7 further presents the Raman spectrums of the GMCMBs and 3DGNs treated with different dosages of $KMnO_4$ at the same heating temperature of 950 °C. Curve a shows the GMCMBs, and curves b-f are the 3DGNs treated with 10 g, 12 g, 14 g, 16 g and 18 g of $KMnO_4$, respectively. Obviously, these samples display obvious characteristic peaks at about 1350 cm^{-1} and 1580 cm^{-1}, corresponding to the G band and D band, respectively. The G band of carbon materials was characterized by the degree of the graphitization, where the stronger the G band indicates the higher the degree of graphitization. The D band represents the structural defects of graphite crystals, which also reflects the intervention of hydroxyl and oxygen functional groups in the material.[19] Usually, the intensity ratio of D band and G band (I_D/I_G) can be used to determine the of disorder degree of graphite material. For the pristine GMCMBs, the G band was high and narrow while the D band was lower and thus the I_D/I_G value was up to 0.20, which indicated that GMCMBs had a good crystals structure of graphite. After treated with $KMnO_4$ and

heated reduction, the I_D/I_G values of 3DGNs were 1.21, 1.19, 1.18, 1.17, 1.18, for 10 g, 12 g, 14 g, 16 g and 18 g of $KMnO_4$, respectively. In addition, at about 2700cm^{-1}, GMCMBs appeared strong graphite 2D band, while the 2D band of 3DGNs all are weaker than that of GMCMBs, indicating the partial SP^2 hybrid carbon is destroyed. The structural defects go together with the existence of oxygen functional groups are confirmed by the EDS (Fig. 2) and FT-IR (Fig. S2). The existence of these functional groups-induced crystal defects can provide more energy storage spaces and transport channels, which is beneficial to improve the electrochemical performance of the electrode material.[20]

Fig. 8 exhibits the SEM images of 3DGNs treated with different dosages of $KMnO_4$ (A, B: 10 g, C, D: 12 g, E, F: 14 g, G, H: 16 g) at the same heating temperature of 950 ^oC. For comparison, the SEM images of GMCMBs are also provided in Fig. S1, which reveal a very good sophericity and highly smooth surface. However, after the oxidation and high-temperature reduction treatment, these GMCMBs show a great deal of deep the large gaps with a horizontal extension, as seen from Fig. 8. When $KMnO_4$ is 10 g, the cracks have appeared, but small number of cracks and relatively thick carbon layers are found. With the increase of the dosages of $KMnO_4$, the deformation of GMCMBs increases, and increasingly clear network-like carbon layers can be observed. Expressly, when $KMnO_4$ was raised to 18 g (see Fig. 1 A-C), ultrathin nanosheet architecture of 3DGNs were finally formed. It is well known that the Hummers oxidation method using strong oxidation agent of $KMnO_4$, can be able to get deep oxidation of graphite, so that the interpolating agent of H_2SO_4 can be more evenly inserted into the carbon layers.[21] In the subsequent process of high-temperature reduction, the interpolating agent can be rapidly took off the carbon layers, in which the carbon layer will be pushed open, therefore contributing the formation of ultrathin graphene-like nanosheets. Based on the above-mentioned findings (including XRD, Raman, SEM and SSA results), one can drew a conclusion that the higher dosage of $KMnO_4$ is beneficial to the development of more desirable 3D interconnected graphene-like nanosheets, due to their deep oxidation and efficient delamination from the oxidation and interpolating agents.

The specific surface areas (SSA) of the samples with different $KMnO_4$ dosages are presented in Table 1. It is obvious that SSA of GMCMBs is only 6.15 m^2/g, while those of 3DGNs are gradually increased with the increase of $KMnO_4$ dosages. When the dosage of $KMnO_4$ is 18 g, the SSA of 3DGNs can reach 180.92 m^2/g, which is nearly 30 times as high as that of GMCMBs. In addition, the tap densities of the samples are also listed in Table 1, which shows the gradually decreasing property opposed to the SSA. At the same time, the nitrogen adsorption-desorption analysis of the samples (Fig. 9 A) exhibits the typical characteristics of mesoporous carbon materials, with increasing adsorption volume as well as pronounced desorption hysteresis loops.[14] The pore diameter distribution (Fig. 9 B) indicates that the samples have the satisfactory mesoporous texture (focused on 3-6 nm). Expressly, for the three samples with 14 g, 16 g and 18 g $KMnO_4$, additional larger mesopores (20-50 nm) and remarkable macropores (50-300 nm) are achieved successfully. It is obvious that the volume and diameter of macropores increases continuously with the increasing of $KMnO_4$ dosages, which suggests that the $KMnO_4$ dosage plays a key role in developing 3D interconnected graphene-like nanosheets with desirable macroporous structures.

Table 1 SSA and Tap density of the samples treated with different $KMnO_4$ dosages at the same heating temperature of 950 ^oC.

$KMnO_4$ dosages (g)	0	10	12	14	16	18
SSA (m^2/g)	6.15	32.77	58.43	105.48	132.75	180.92
Tap density (g/cm^3)	1.83	0.52	0.29	0.17	0.13	0.09

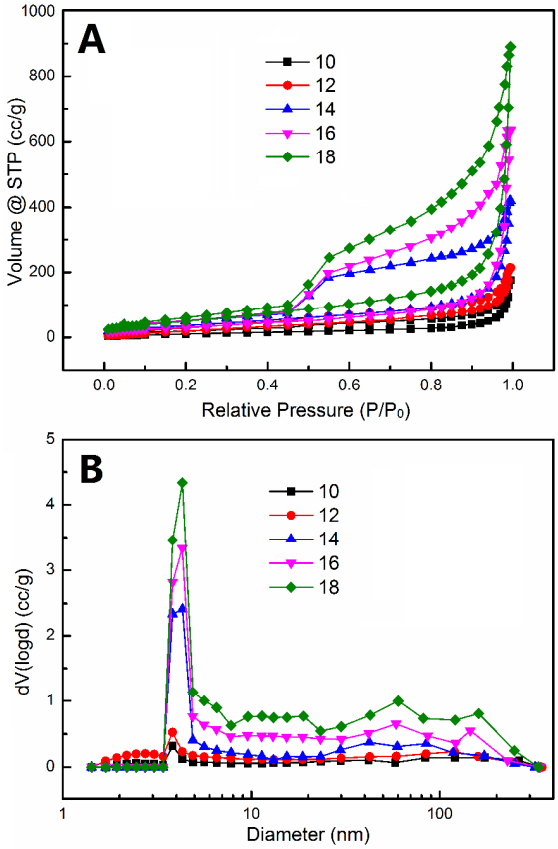

Fig. 9 Nitrogen adsorption-desorption isotherm (A) and pore diameter distribution (B) of samples treated with different $KMnO_4$ dosages (10 g, 12 g, 14 g, 16 g and 18 g) at the same heating temperature of 950 ^oC.

The electrochemical performances of the GMCMBs sand 3DGNs treated with different $KMnO_4$ dosages were evaluated using deep galvanostatic charge/discharge cycles between 3.00-0.01 V at a current density of 0.1 A/g. The lithium storage capacities of the anodes were calculated based on the mass of bare GMCMBs or the mass of bare 3DGNs. The first, second and fifth charge/discharge voltage profiles are shown in Fig. 10. For the GMCMBs (Fig. 10 A), the voltage drops quickly with the increase of discharge capacity from 3.00 V to 0.25 Vs, suggesting its lower specific surface area. And a long discharge platform appears after 0.25 V, which reflects the intercalating process of Li^+ into graphite layers, being the main lithium storage process of graphite materials.[17] However, for the 3DGNs samples (Fig. 10 B-F), all the voltage drops slowly with the increase of discharge capacity in the whole voltage range, which is a typical lithium storage property of graphene-based materials with higher specific surface area.[3] The GMCMBs deliveres discharge capacities of 483.4, 369.0 and 362.7 mAh/g at the first, second and fifth cycles, respectively. The results are very close to the theoretical capacity of 372 mAh/g for graphite materials. The 3DGNs (10 g) (10

g $KMnO_4$) shows obviously improved discharge capacities of 956.4, 540.3 and 513.6 mAh/g at first, second and fifth cycles, respectively. The discharge capacities of the 3DGNs increased gradually with the increase of the dosages of $KMnO_4$. Remarkably, the discharge capacities of the 3DGNs (18 g) raise as high as 6352.3, 2795.6 and 2240.7 mAh/g at the first, second and fifth cycles, respectively. Compared with previous reports,[3] these results are geared to very high capacity values for the graphene-based materials. Besides, the Coulombic efficiency in the first charge/discharge are 81.6%, 56.5%, 56.2%, 48.7%, 42.4% and 46.2%, for GMCMBs, 3DGNs (10g), 3DGNs (12g), 3DGNs (14g), 3DGNs (16g), 3DGNs (18g), respectively. The Coulombic efficiency of 3DGNs (18g) in the second and fifth cycles can reach 88.7% and 94.5%, respectively, which are very close to those of GMCMBs (second cycle for 89.2% and fifth cycle for 95.6%). These results suggest that an acceptable efficiency of the present sample can be achieved by an appropriate electrochemical activation.

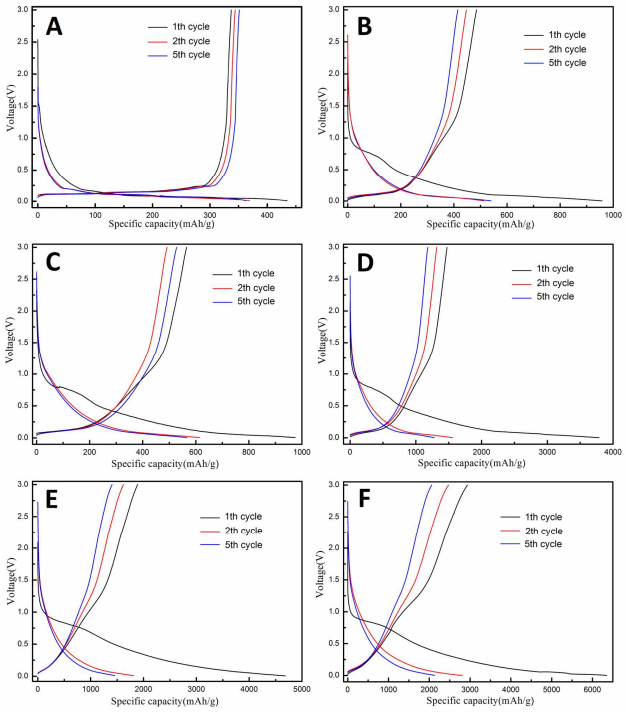

Fig. 10 Galvanostatic charge/discharge profiles of the GMCMBs (A) and 3DGNs (B-F) treated with different $KMnO_4$ dosages (B: 10 g, C: 12 g, D: 14 g, E: 16 g, F: 18 g) at the same heating temperature of 950 °C.

In order to further investigate the electrochemical stability of the 3DGNs electrodes, continuous charge/discharge cycling test in 120 times at the current density of 0.1 A/g is also implemented, and the result is shown in Fig. 11. It can be seen that all these electrodes display relatively stable performances for the lithium storage. Particularly, the 3DGNs (18g) exhibits much higher discharge capacity than other electrodes in the whole cycling, in which very high capacity values of 1865.3 and 1708.5 mAh/g are achieved after the 60 and 120 cycles, respectively. These attractive capacity values along with a well retention rate suggest that the 3DGNs architecture is of a very fascinating application prospect for high-performance LIBs. On the other hand, the Nyquist plots from the electrochemical impedance spectroscopy (before and after charge/discharge cycling) for the 3DGNs sample are presented in Fig. 12. From the Fig. 12 A, it can be seen that, before the cycling test the resistance values of 3DGNs (10g), 3DGNs (12g), 3DGNs (14g), 3DGNs (16g), 3DGNs (18g) are 97, 121, 145, 172, 248 Ω, respectively. After the 120 times of charge/discharge cycling, resistance values for all these samples are greatly reduced due to the sufficient interaction of active material and electrolytic solution. For example, resistance value of 3DGNs (18g) is down to 54 Ω after the cycling test, which demonstrates that lower inner resistance and desirable electronic conductivity can be obtained for the 3DGNs samples during lithium storage process.

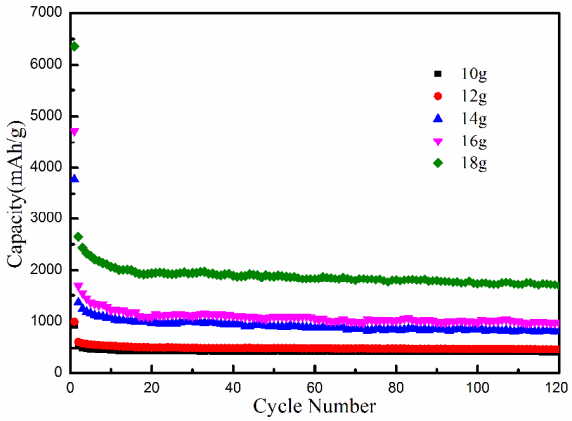

Fig. 11 Discharge cycling profiles at 0.1 A/g of the as-prepared 3DGNs samples with different $KMnO_4$ dosages at the same heating temperature of 950 °C.

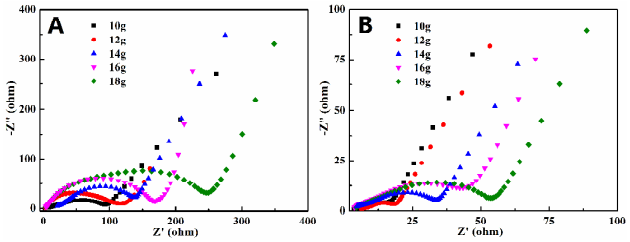

Fig. 12 Electrochemical impedance spectras of 3DGNs samples (A) before and (B) after 120 times of continuous charge/discharge cycling.

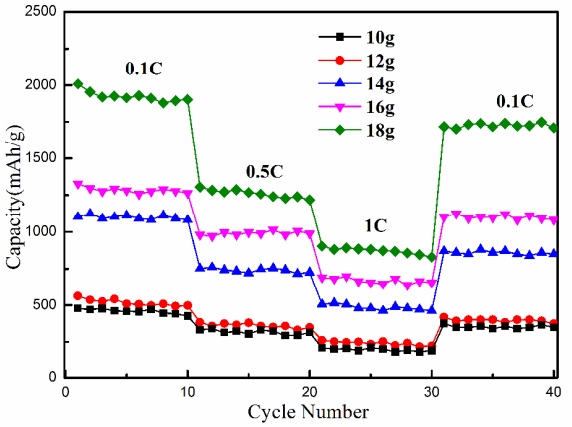

Fig. 13 The rate capability of the as-prepared 3DGNs samples with different $KMnO_4$ dosages at the same heating temperature of 950 °C.

The rate performances of the electrodes of 3DGNs with different $KMnO_4$ dosages are compared in Fig. 13. These cells are first cycled at a rate 0.1 C, and then the rate is increased to 0.5 and 1.0 C, finally increased to 0.1 C, successively. As expected, the capacity decreases with the increasing rates and in increases again after the recovery of rates. Furthermore, the capacity is relatively stable at each rate for all these electrodes. It is noteworthy that 3DGNs (18g) demonstrates the most excellent lithium storage capacity at each rate, when comparing with the other electrodes. With the increasing of rates (0.1, 0.5, 1.0 C), the capacities at the end of each rate are measured for 1903.5, 1217.8 and 829.2 mAh/g, respectively. When the rate returns to 0.1 C, the capacity recovers to be 1716.3 mAh/g and retain as high as 1709.8 mAh/g at end of 40 times of cycling. These results prove that the as-prepared 3DGNs electrodes possess high rate capability for application of lithium ion battery.

Graphene has a theoretical discharge capacity of 372 mAh/g, pass through the formation of LiC_6 with a single-sided Li adsorption, or 744 mAh/g when Li ions are adsorbed on both sides of graphene.[22] However, the experimental the discharge capacity of graphite-based anode can exceed one thousand even thousands by means of material design and functionalization.[23] For example, the randomly stacked holey graphene electrode produced a very high discharge capacity of 2207 mAh/g.[24] Particularly, the 3D porous graphene network[25] and mesoporous graphene nanosheets[26] electrodes displayed the higher capacities of about 2300 and 3500 mAh/g, respectively. The greatly improved lithium storage capacity originated from the advantageous nanostructure of the graphene materials with larger surface areas and substantial nanopores for lithium adsorption.[24-26] On the other hand, the recently developed heteroatom-doping (e.g. O, N and B atoms) graphene electrodes demonstrated a new and promising strategy for designing ultra-high capacity electrodes for the lithium ion batteries, because the heteroatom doping could be instrumental to optimally balance Li storage and diffusion for graphene electrodes.[27]

With regard to the high capacity (about 2800 mAh/g reversible capacity) of lithium storage for the 3DGNs, several possible reasons have been summarized as follows. Firstly, as a result of deep oxidation and high temperature reduction, the interlayer space and specific surface area of the graphite material increased obviously, which provides more abundant active sites for the lithium storage.[3] Secondly, the satisfactory mesoporous structure (focused on 3-6 nm) is considered to be beneficial to the lithium ion adsorption.[24] Thirdly, the 3DGNs there are a large number of oxygen functional groups (C=O, O-H, C-O-C, etc.) which can contribute to the additional high capacity via Faradaic reaction with Li, for example, $Li^+ + C{=}O + e^- \Leftrightarrow C\text{-}O\text{-}Li$.[28] Fourthly, the latent crystal defects in graphene endows with more lithium storage space and transport channels.[20] It also prevents clustering of Li by the strong interaction between Li and defect sites.[29] Fifthly, it is suggested that the ultrathin graphene-like nanosheets-built 3D network architecture and the graphene layers with disordered curly structures both possess extraordinary lithium storage capability.[5, 6] Finally, their binary channels for the electron transport and diffusion of ions are also the advantageous factors for the enhanced lithium storage with high rate capacity.[7,14] On the other hand, the desirable electrochemical stability of the 3DGNs electrode can be supported by the viewpoint that the 3D network architectures have been preventing the graphene nanosheets from aggregating.[5, 6]

Conclusions

In summary, we demonstrated a high-efficiency production of three-dimensional interconnected graphene-like nanosheets (3DGNs) for anode material of LIBs, through a facile chemical oxidation-thermal expansion associated strategy. The strategy allowed straightforward evolvement of GMCMBs into 3DGNs, without the help of additional self-assembly or templet-orientation processes. Because of the deep oxidation of $KMnO_4$ and the rapidly thermal reduction, efficient delamination of graphite microspheres into ultrathin graphene-like nanosheets was readily achieved. The results suggested that the dosage of $KMnO_4$ is an important factor for the development of 3D macroporous network architecture of the 3DGNs. When evaluated the electrochemical performances as anode material of LIBs, the electrode of 3DGNs architecture demonstrates surprisingly improved electrochemical performances with discharge capacities of 6352.3, 2795.6 and 2240.7 mAh/g at the first, second and fifth cycles, respectively. Moreover, a desirable electrochemical stability is also demonstrated. The 3DGNs product would be one of candidate anode materials for high-performance LIBs used for up-to-date portable electronics and hybrid power systems.

Acknowledgements

Financial supports from National Natural Science Foundation of China (U1401246, 51474110, 51474077 and 21443006) and Provincial Natural Science Foundation of Guangdong (2014A030310179) are gratefully acknowledged.

Notes and references

1 (a) Y. X. Tang, Y. Y. Zhang, W. L. Li, B. Ma and X. D. Chen, *Chem. Soc. Rev.,* 2015, **44**, 5926-5940 F. (b) Y. Zhao, X. F. Li, B. Yan, D. Li, S. Lawes, X. L. Sun, J. Power Sources, 2015, **274**, 869-884.

2 (a) A. D. Roberts, X. Li and H. F. Zhang, *Chem. Soc. Rev.,* 2014, **43**, 4341-4356. (b) Y. L. Li, J. J.Wang, X. F. Li, J. Liu, D. S. Geng, J. L. Yang, R. Y. Li, X. L. Sun, *Electrochem. Commun.*, 2011, **13**, 668-672.

3 (a) X. F. Li, Y. H. Hu, J. Liu, A. Lushington, R.Y. Lia, X. L. Sun, *Nanoscale*, 2013, **5**, 12607-12615. (b) M. Srivastava, J. Singh, T. Kuila, R. K. Layek, N. H. Kime and J. H. Lee, *Nanoscale,* 2015, **7**, 4820-4868.

4 (a) B. Jang, O. B. Chae, S. K. Park, J. Ha, S. M. Oh, H. B. Na and Y. Piao, *J. Mater. Chem. A*, 2013, **1**, 15442-15446. (b) R. Guo, L. Zhao and W. B. Yue, *Electrochim. Acta*, 2015, **152**, 338-344. (c) Z. J. Fan, J. Yan, G. Q. Ning, T. Wei, L. J. Zhi and F. Wei, *Carbon*, 2013, **60**, 558-561. (d) D. Li, D. Q. Shi, Z. X. Chen, H. K. Liu, D. Z. Jia and Z. P. Guo, *RSC Adv.*, 2013, **3**, 5003-5008.

5 (a) Y. X. Xu, G. Q. Shi and X. F. Duan, *Acc. Chem. Res.*, 2015, **48 (6)**, 1666-1675. (b) Y. Y. Li, Q. W. Zhang, J. L. Zhu, X. L. Wei and P. K. Shen, *J. Mater. Chem. A*, 2014, **2**, 3163-3168. (c) Y. Y. Li, Z. S. Li, Q. W. Zhang and P. K. Shen, *J. Mater. Chem. A*, 2014, **2**, 4528-4533. (d) M. Zhang, Y. Wang and M. Q. Jia, *Electrochim. Acta,* 2014, **129**, 425-432.

6 C. Li and G. Q. Shi, *Nanoscale*, 2012, **4**, 5549-5563.

7 (a) C. G. Hu, H. H. Cheng, Y. Zhao, Y. Hu, Y. Liu, L. M. Dai and L. T. Qu, *Adv. Mater.*, 2012, **24 (40)**, 5493-5498. (b) J. J. Liu, W. Lv, W. Wei, C. Zhang, Z. J. Li, B. H. Li, F. Y. Kang and Q. H. Yang, *J. Mater. Chem. A*, 2014, **2**, 3031-3037.

8 (a) X. H. Xia, D. L. Chao, Y. Q. Zhang, Z. X. Shen and H. J. Fan, *NanoToday*, 2014, **9 (6)**, 785-807. (b) X. H. Cao, Z. Y. Yin and H. Zhang, *Energy Environ. Sci.*, 2014, **7**, 1850-1865.

9 S. Nardecchia, D. Carriazo, M. L. Ferrer, M. C. Gutiérreza and F. Monte, *Chem. Soc. Rev.*, 2013, **42**, 794-830.

10 Y. X. Xu, K. X. Sheng, C. Li and G. Q. Shi, *ACS Nano*, 2010, **4 (7)**, 4324-4330.

11 (a) L. Ren, K. S. Hui and K. N. Hui, *J. Mater. Chem. A*, 2013, **1**, 5689-5694. (b) C. Jiang, B. Zhao, J. Y. Cheng, J. Q. Li, H. J. Zhang, Z. H. Tang and J. H. Yang, *Electrochim. Acta,* 2015, **173**, 399-407.
12 B. G. Choi, M. H. Yang, W. H. Hong, J. W. Choi and Y. S. Huh, *ACS Nano,* 2012, **6 (5)**, 4020-4028.
13 Z. P. Chen, W. C. Ren, L. B. Gao, B. L. Liu, S. F. Pei and H. M. Cheng, *Nat. Mater.*, 2011, **10**, 424-428.
14 Y.Y. Li, Z. S. Li and P. K. Shen, *Adv. Mater.*, 2013, **25 (17)**, 2474-2480.
15 (a) S. Li, X. Y. Qin, H. R. Zhang, J. X. Wu, Y. B. He, B. H. Li and F. Y. Kang, *Electrochem. Commun.*, 2014, **49**, 98-102. (b) Y. R. Ren, H. M. Wei, B. Yang, J. W. Wang and J. N. Ding, *Electrochim. Acta*, 2014, **145**, 193-200.
16 (a) Y. Bian, Z. Y. Bian, J. X. Zhang, A. Z. Ding, S. L. Liu and H. Wang, *Appl. Surf. Sci.*, 2015, **329**, 269-275. (b) M. C. Hsiao, S. H. Liao, M. Y. Yen, P. I. Liu, N. W. Pu, C. A. Wang and C. C. M. Ma, *ACS Appl. Mater. Interfaces*, 2010, **2 (11)**, 3092-3099.
17 X. Y. Cao, J. H. Kim and S. M. Oh, *Electrochim. Acta*, 2002, **47**, 4085-4089.
18 L. Song, F. Khoerunnisa, W. Gao, W. H. Dou, T. Hayashi, K. Kaneko, M. Endo and P. M. Ajayan, *Carbon*, 2013, **52**, 608-612.
19 (a) K. Davami, M. Shaygan, N. Kheirabi, J. Zhao, D. A. Kovalenko, M. H. Rümmeli, J. Opitz, G. Cuniberti, J. S. Lee and M. Meyyappan, *Carbon*, 2014, **72**, 372-380. (b) R. Trusovas, K. Ratautas, G. Račiukaitis, J. Barkauskas, I. Stankevičienė, G. Niaura and R. Mažeikienė. *Carbon*, 2013, **52 (2)**, 574-582.
20 (a) W. Lee, S. Suzuki and M. Miyayam, *Electrochim. Acta*, 2014, **142**, 240-246. (b) C. Zheng, X. F. Zhou, H. L. Cao, G. H. Wang and Z. P. Liu *J. Mater. Chem. A*, 2014, **2**, 7484-7490.
21 W. S. Hummers Jr. and R. E. Offeman, *J. Am. Chem. Soc.*, 1958, **80 (6)**, 1339-1339.
22 (a) G. Wang, X. Shen, J. Yao, J. Park, *Carbon*, 2009, **47**, 2049-2053. (b) R. Mukherjee, A. V. Thomas, A. Krishnamurthy, N. Koratkar, *ACS Nano*, 2012, **6**, 7867-7878.
23 H. P. Cong, J. F. Chen, S. H. Yu, *Chem. Soc. Rev.*, 2014, **43**, 7295-7325.
24 Z. Jiang, B. Pei, A. Manthiram, *J. Mater. Chem. A*, 2013, **1**, 7775-7781.
25 Z. L. Wang, D. Xu, H. G. Wang, Z. Wu, X. B. Zhang, *ACS Nano*, 2013, **7** 2422-2430.
26 Y. Fang, Y. Lv, R. Che, H. Wu, X. Zhang, D. Gu, G. Zheng, D. Zhao, *J. Am. Chem. Soc.*, 2013, *135*, 1524-1530.
27 X. Wang, G. Sun, P. Routh, D. Kim, W. Huang, P. Chen, *Chem. Soc. Rev*., 2014, *43*, 7067-7098.
28 S. W. Lee, N. Yabuuchi, B. M. Gallant, S. Chen, B. S. Kim, P. T. Hammond, Y. Shao-Horn, Nat. Nanotechnol., 2010, 5, 531-537.
29 D. Das, S. Kim, K. R. Lee, A. K. Singh, Phys. *Chem. Chem. Phys.*, 2013, **15**, 15128-15134.